SIAM J. SCI. COMPUT.
Vol. 43, No. 3, pp. A2352–A2380

A LEVEL-SET ADJOINT-STATE METHOD FOR TRANSMISSION TRAVELTIME TOMOGRAPHY IN IRREGULAR DOMAINS*

SHINGYU LEUNG†, JIANLIANG QIAN‡, AND JIANGTAO HU§

Qian would like to dedicate this paper to Professor Robert Burridge on the occasion of his 80th birthday for his many pioneering works on geometrical optics and wave motion!

Abstract. We propose an efficient PDE based approach for solving the first-arrival traveltime tomography problem in irregular domains. We consider the mismatch functional based on the L_1 or L_2 fidelity term, respectively, and we compute both functional gradients with respect to the sound speed by the adjoint-state method. The novelty of the proposed method consists of two aspects. First, since the tomography problem is formulated in an irregular domain, we develop new efficient level-set based fast sweeping methods for solving the eikonal and adjoint-state equations in the irregular domain. Second, since the computed adjoint state is associated with a source singularity originated from the gradient of a point source eikonal solution, we propose a novel decomposition approach to remove this singularity, which just requires solving the same adjoint-state equation again but with a different boundary condition. Finally, we show the performance of the proposed algorithm on several numerical examples including a synthetic data set from ultrasound computerized tomography.

Key words. inverse problem, eikonal equation, adjoint state, traveltime tomography, irregular domain

AMS subject classifications. 78A05, 78A46, 78M35

DOI. 10.1137/20M1383082

1. Introduction.

As an important class of inverse problems, traveltime tomography arises from a variety of applications, such as seismic imaging, medical imaging, nondestructive testing, and underwater acoustics. Given traveltime data between sources and receivers, traveltime tomography posed as an inverse problem is to recover the sound speed of an underlying interior medium between sources and receivers from traveltime measurements. Since there may exist multiple ray paths to connect a source and a receiver, traveltime tomography may be formulated as first-arrival (single-arrival) or multiarrival inverse problems, which correspond to boundary rigidity or lens rigidity problems in differential geometry, respectively. In this paper, given first-arrival traveltime boundary data, we develop a normalized adjoint-state level-set method for eikonal based traveltime tomography in irregular domains.

In medical imaging, ultrasound computed traveltime tomography uses time-of-flight data between transducers and receivers to invert for the speed of sound [11]; the resulting speed of sound can be further used in photoacoustic tomography to compensate for acoustic heterogeneities [14]. In seismic imaging, traveltime tomography is an

*Submitted to the journal's Methods and Algorithms for Scientific Computing section November 30, 2020; accepted for publication (in revised form) April 16, 2021; published electronically June 28, 2021.

https://doi.org/10.1137/20M1383082

Funding: The work of the first author was partially supported by Hong Kong RGC grants 16303114 and 16309316. The work of the second author was partially supported by the National Science Foundation. The work of the third author was partially supported by the National Natural Science Foundation of China through grants 42074166 and U1562219.

†Department of Mathematics, Hong Kong University of Science and Technology, Clear Water Bay, Hong Kong (masyleung@ust.hk).

‡Department of Mathematics, Michigan State University, East Lansing, MI 48824 USA (qian@math.msu.edu).

§State Key Lab of Oil and Gas Reservoir Geology and Exploration (Chengdu University of Technology), Erxiangqiao, Chengdu 610059, Sichuan, People's Republic of China (jiangtao_hu@126.com).

essential method for obtaining subsurface velocity models so that seismic migration can be carried out or full waveform inversion can be initialized [19, 43]. Most of these available traveltime tomography methods are either based on Lagrangian ray-tracers or based on Eulerian eikonal solvers.

Traditional traveltime tomography methods mostly rely on ray-tracing to compute traveltimes between sources and receivers so as to fit the traveltime data [30]. Ray-tracing based approaches have at least two shortcomings: first, since the Hamiltonian system for computing ray paths is very sensitive to initial conditions and it is generally difficult to control where a ray goes, it is a nontrivial task to assign traveltimes from a source to all receivers by ray-tracing in numerical simulations; second, Fermat-principle based shooting methods for two-point boundary value problems between a source and a receiver may fail to converge. Consequently, some alternative methods are sought to avoid explicit ray-tracing.

Based on the eikonal solvers for first-arrival traveltimes [47], Ammon and Vidale [1] developed a traveltime tomography method without rays by computing explicitly the discretized Frechet derivative of first-arrival traveltime with respect to sound speed. To avoid computing Frechet derivatives directly, Sei and Symes [36, 37] proposed an adjoint-state method for traveltime tomography based on paraxial eikonal equations. Later on, Leung and Qian [19] developed adjoint state methods systematically for traveltime tomography based on eikonal equations. Because it enjoys a simple implementation, low computational cost, and low memory requirement, this adjoint state method has been further developed in [43, 15, 22, 23]. The success of all these eikonal based first-arrival traveltime tomography methods heavily relies on robust and efficient eikonal solvers which have been extensively developed in the last two decades [47, 46, 35, 38, 32, 52, 45, 16, 50, 33, 34, 17, 13, 26, 24].

Nevertheless, most implementations of eikonal solver tomography methods are based on finite-difference meshes of rectangular domains [19, 43, 15, 22, 23], which may hinder their applications to problems posed in irregular domains. In this work, we develop a level-set based fast sweeping method for eikonal based adjoint-state traveltime tomography, which is able to handle irregular domains naturally.

Moreover, since an eikonal solver based traveltime tomography method usually solves an adjoint-state equation to define an updating gradient which is singular at the source point, the resulting velocity model is in fact singular at the source point; consequently, the final reconstruction result is of low resolution and has some kind of "footprint" near the source point. Such a singularity is actually linked to that of the underlying traveltime field. Since solving the point source isotropic eikonal equation intrinsically corresponds to emanating rarefaction rays from the source point, the resulting traveltime gradient is singular at the source point, and we dub such a singular pattern the imprint of ray illumination. Because the adjoint state equation propagates traveltime residuals back to the source point according to the negative traveltime gradient, the resulting adjoint state will inherit such an imprint of ray illumination, leading to singular gradient descent directions when updating the velocity model in the adjoint-state traveltime tomography. To mitigate this imprint, we propose to solve the adjoint state equation twice but with different boundary conditions, one being taken to be regular data residuals, and the other taken to be ones uniformly, so that we are able to use the latter adjoint state to normalize the regular one and we further use the normalized quantity to serve as the gradient direction to update the velocity model. We mention that a similar idea has been used in [3] for estimating the Hessian of the misfit functional with respect to the slowness. Although our formulation is

analogous to that in [3], our mathematical understanding of the problem is different. We will show the mathematical meaning of this normalized quantity.

Theoretically, viewed as a boundary rigidity problem, first-arrival traveltime tomography consists in determining a compact Riemannian manifold with boundary up to an action of a diffeomorphism which is the identity at the boundary by knowing the geodesic distance function between boundary points (see [28, 29, 27, 31, 39] and references therein). One needs an a priori hypothesis to do so since it is easy to find counterexamples if the speed of sound is too low in certain regions. An a priori condition that has been proposed is simplicity of the metric [27]. A manifold is simple if the boundary is strictly convex with respect to the Riemannian metric and there are no conjugate points along any geodesic. So far it seems to be difficult to handle the case with conjugate points since they are related to the so-called caustics and multiarrivals in geometrical optics [39, 40, 41]. In practice, we do not know in advance whether the Riemannian metric defined by the underlying sound speed is simple or not. Consequently, the available first-arrival traveltime information may not suffice to determine the sound speed so that the resulting sound speed model may have limited resolution when the to-be-imaged structure is very complicated, and this can be observed in numerical results for the Marmousi model as shown in [12]. To improve resolution of traveltime tomography, we have to take into account multiarrivals as demonstrated in [20, 7, 8, 53].

The rest of the paper is organized as follows. Section 2 summarizes the adjoint-state method for traveltime tomography and develops the algorithm for removing the singularity of adjoint variables due to the singularity of a point source. Section 3 gives implementation details of algorithms for the normalized adjoint-state method of traveltime tomography in irregular domains. In section 4 we carry out various numerical experiments to demonstrate effectiveness of the proposed new algorithm. Section 5 concludes the paper with some remarks.

2. Mathematical formulations.

2.1. Background. We start from the eikonal equation with a point source condition in an isotropic medium which occupies an open and bounded domain Ω_p enclosed by a rectangular domain $\Omega_p \cup \Omega_e$; see Figure 1. By isotropy here we mean the wave velocity has no directional dependence. The eikonal equation is

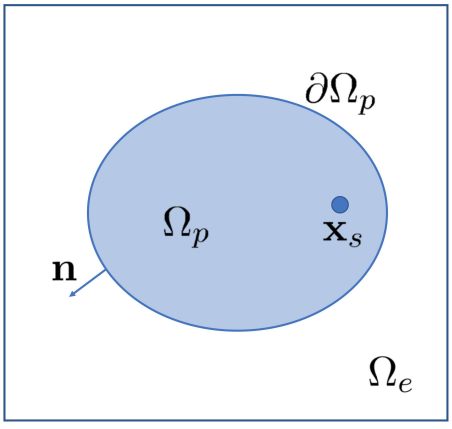

FIG. 1. *Setup of the inverse problem.*

$$|\nabla T| = \frac{1}{c} \tag{2.1}$$

with the point source condition

$$T(\mathbf{x}_s) = 0\,, \tag{2.2}$$

where $T(\mathbf{x})$ is the traveltime of wave from the source $\mathbf{x}_s$ to the point $\mathbf{x} = (x, z)$, and $c \in C^1(\Omega)$ is a positive velocity function. For a given velocity model c, the viscosity solution of this equation can be computed efficiently by fast sweeping methods, and such solutions correspond to the least traveltime or the first-arrival traveltime according to [25].

In this work we are interested in the related inverse problem, the so-called transmission traveltime tomography problem: given both the first-arrival travel-time measurements on the boundary $\partial\Omega_p$ and the location of the point source $\mathbf{x}_s \in \Omega_p$, invert for the velocity field $c(\mathbf{x})$ inside the domain Ω_p.

To achieve this, two of the authors proposed in [19] to invert for the velocity model by minimizing the following mismatching functional (energy):

$$E(c) = \frac{1}{2}\int_{\partial\Omega_p} |T - T^*|^2 d\Gamma\,, \tag{2.3}$$

where $T^*|_{\partial\Omega_p}$ is the measurement and $T|_{\partial\Omega_p}$ is computed by solving (2.1) with a point source condition (2.2). In other words, this energy measures the L^2-difference between the experimental measurement, T^*, and the solution from the eikonal equation, T, on the boundary of the computational domain.

To minimize this energy, we use the method of gradient descent. We first perturb the velocity field c by $\epsilon\tilde{c}$, which causes a corresponding change in T by $\epsilon\tilde{T}$. The change in the energy is then given by $\delta E = \epsilon\int_{\partial\Omega_p}\tilde{T}(T-T^*)+O(\epsilon^2)$. From the state equation (2.1), the perturbations in c and T are related by $\nabla T\cdot\nabla\tilde{T} = -\tilde{c}/c^3$. To efficiently compute $\tilde{c}$ which minimizes E, we propose to use the adjoint state method as in [19]. The idea is to introduce an adjoint variable λ satisfying

$$\nabla\cdot(\lambda\nabla T) = 0\,, \tag{2.4}$$

with the boundary condition,

$$(\mathbf{n}\cdot\nabla T)\lambda = T^* - T, \tag{2.5}$$

on the boundary $\partial\Omega_p$, where $\mathbf{n}$ is the unit outward normal of the boundary. Ignoring the higher than linear order terms in the energy perturbation, we have

$$\frac{\delta E}{\epsilon} = \int_{\Omega_p}\frac{\tilde{c}\lambda}{c^3}d\mathbf{x}\,.$$

Finally, the energy is minimized using the method of gradient descent, and one could choose the perturbation $\tilde{c} = -\lambda/c^3$. This implies that $\delta E = -\epsilon\int_{\Omega_p}\tilde{c}^2 d\mathbf{x} \le 0$ and the equality holds when $||\tilde{c}||_{H^0(\Omega_p)} = 0$. However, it is not straightforward how one can guarantee the following two properties:

1. $\tilde{c}^k|_{\partial\Omega_p} = 0$;
2. $c^{k+1} = c^k + \epsilon\tilde{c}^k$ smooth.

The first condition assumes that we know c on the boundary $\partial\Omega_p$, denoted by $c^*|_{\partial\Omega_p}$, which is a reasonable assumption. This means that the variations of the velocity function on the boundary should be zero. The second condition is a regularity condition on c^k. This regularity seems to be too restrictive in practice. In general, one only needs $c^k \in C^1$ to guarantee well-posedness of the state equation (2.1). However, assuming that one uses $\tilde{c}^k = -\lambda/\left(c^k\right)^3$ directly, it is not clear whether this function would give us the desired regularity. Even if this perturbation is in C^1, the numerical solution may have jumps or spikes. These irregularities will force one to pick a very small step-size, ϵ^k, in the minimization process. Therefore, to have faster convergence, we impose the above regularity in each iteration.

Following [19], we use the descent direction

$$\tilde{c} = -(I - \nu\Delta)^{-1}\left(\frac{\lambda}{c^3}\right), \tag{2.6}$$

where I is the identity operator, Δ is the Laplacian operator, and $\nu \geq 0$ controls the amount of regularity that one wants. The homogeneous boundary condition is imposed in inverting the operator $(I - \nu\Delta)$. With this particular $\tilde{c}$, we have $\delta E = -\epsilon \int_{\Omega_p} (\tilde{c}^2 + \nu|\nabla\tilde{c}|^2) \leq 0$.

2.2. Removing the singularity in adjoint-state solutions. Since solving the point-source isotropic eikonal equation intrinsically corresponds to emanating rarefaction rays from the source point, the resulting traveltime gradient is singular at the source point, and we dub such a singular pattern the imprint of ray illumination.

Because the adjoint state equation propagates traveltime residuals back to the source point according to the negative traveltime gradient, the resulting adjoint state will inherit such an imprint of ray illumination, leading to singular gradient descent directions when updating the velocity model in the adjoint-state traveltime tomography.

To mitigate this imprint, we propose to solve the adjoint state equation twice but with different boundary conditions: one being taken to be regular data residuals, and the other taken to be ones uniformly, so that we are able to use the latter adjoint state to normalize the regular one and we further use the normalized quantity to serve as the gradient direction to update the velocity model.

The idea is the following. To carry out traveltime tomography, we need to solve the following adjoint state equation after solving the eikonal equation:

$$-\nabla \cdot (\lambda \nabla T) = 0, \tag{2.7}$$

$$\frac{\partial T}{\partial \mathbf{n}}\lambda|_{\partial\Omega_p} = f, \tag{2.8}$$

where f is the traveltime residual. We denote λ^f the solution of this equation.

To normalize the singular behavior of the adjoint state, we propose to solve the adjoint state equation (2.7) once more with a different boundary condition,

$$\frac{\partial T}{\partial \mathbf{n}}\lambda|_{\partial\Omega_p} = 1, \tag{2.9}$$

and we denote the resulting solution to be λ^1.

Next we propose to normalize λ^f by λ^1 so that we have a new function

$$\beta(\mathbf{x}) = \frac{\lambda^f(\mathbf{x})}{\lambda^1(\mathbf{x})}. \tag{2.10}$$

To validate this normalization procedure, we next prove that β is nonsingular.

We start from the following lemma.

LEMMA 1 ([2, 42]). *For the eikonal equation* (2.1) *with the point source condition* (2.2)*, there exists a neighborhood of the source* $\mathbf{x}_s$ *through each point* $\mathbf{x}$ *of which, other than the source itself, there passes one and only one ray so that the eikonal solution* $T(\mathbf{x};\mathbf{x}_s)$ *at point* $\mathbf{x}$ *is well defined, and the ray direction at point* $\mathbf{x}$ *is given by* $\nabla_{\mathbf{x}} T(\mathbf{x};\mathbf{x}_s)$.

Assume that Lemma 1 holds in a domain under consideration. Then in such a domain, we introduce ray coordinates in the following sense:

$$(\mathbf{t}_0, \tau) \to \mathbf{x} = \mathbf{x}(\mathbf{t}_0, \tau), \tag{2.11}$$

where for a given unit vector $\mathbf{t}_0$ the curve $\mathbf{x}(\mathbf{t}_0, \tau)$ parametrized by the arc length s or τ with $ds = c\,d\tau$ is the ray emanating from $\mathbf{x}_s$ with direction $\mathbf{t}_0$. Both s and τ are taken to be zero at the source $\mathbf{x}_s$.

LEMMA 2 (conservation for a field parallel to the rays). *Assume that Lemma* 1 *holds in a domain under consideration. Let* $\mathbf{t}$ *be the unit vector tangent to a typical ray emanating from the source* $\mathbf{x}_s$*. Consider the vector field* $V\mathbf{t}$ *parallel to* $\mathbf{t}$ *representing the flux of a conserved quantity. Then the conservation equation*

$$\nabla \cdot (V\mathbf{t}) = 0 \tag{2.12}$$

implies that $V(\tau)$ *is inversely proportional to* $d\sigma(\tau)$ *the cross-sectional area of an infinitesimal tube of rays surrounding the given ray at* τ*, where ray coordinates are used.*

Proof. Let us integrate the conservation equation (2.12) over a volume interior to a narrow tube G of rays terminated at the ends by wave fronts $\tau = \tau_0$ and τ_1, i.e., surfaces everywhere normal to the field of rays. Note that $ds = c\,d\tau$. Then, writing $d\sigma$ for the area element on a section $\sigma(\tau)$ of the tube of rays by the wave front $\tau =$ constant, we may write $d\mathbf{x} = c\,d\sigma d\tau$. So

$$\begin{aligned} 0 \;=\; \int_G \nabla \cdot (V\mathbf{t}) d\mathbf{x} &= \int_{\tau_0}^{\tau_1} \int_{\sigma(\tau)} \nabla \cdot\, (V\mathbf{t})\, c\, d\sigma\, d\tau \\ &= \int_{\partial G} \mathbf{m} \cdot (V\mathbf{t}) dS \\ &= \int_{\sigma(\tau_1)} V d\sigma - \int_{\sigma(\tau_0)} V d\sigma\,, \end{aligned} \tag{2.13}$$

where $S = \partial G$, and $\mathbf{m}$ is the unit outward normal to the ray tube G: $\mathbf{m}$ is parallel to $\mathbf{t}$ in the transverse section of the ray tube and is perpendicular to $\mathbf{t}$ in the longitudinal section of the ray tube.

It follows from the arbitrariness of the cross section of the tube of rays (or by letting the cross section shrink to an area of very small diameter) that

$$0 \;= V(\tau_1) d\sigma(\tau_1) - V(\tau_0) d\sigma(\tau_0)\,, \tag{2.14}$$

so that

$$\frac{V(\tau_1)}{V(\tau_0)} = \frac{d\sigma(\tau_0)}{d\sigma(\tau_1)}. \tag{2.15}$$

Therefore, along a ray, $V(\tau)$ is inversely proportional to $d\sigma(\tau)$ the cross-sectional area of an infinitesimal tube of rays surrounding the given ray at τ. ∎

We have the following theorem, which is one of the main results of the paper.

THEOREM 1. *Assume that Lemma* 1 *holds. The function* β *defined in formula* (2.10) *is nonsingular.*

Proof. Since Lemma 1 holds, we let $(\mathbf{t}_0, \tau_0)$ correspond to a boundary point at $\mathbf{x}_0$ and let $(\mathbf{t}_0, \tau_1)$ correspond to an interior point at $\mathbf{x}_1$, where $\mathbf{x}_1$ and $\mathbf{x}_0$ are connected by the unique ray with the tangent $\nabla_{\mathbf{x}} T(\mathbf{x}(\mathbf{t}_0, \tau); \mathbf{x}_s)$. Applying Lemma 2 with $\mathbf{t} = c\nabla_{\mathbf{x}} T$ and $V = \frac{\lambda}{c}$, we have

$$\frac{\lambda(\tau_1)}{\lambda(\tau_0)} = \frac{c(\tau_1) d\sigma(\tau_0)}{c(\tau_0) d\sigma(\tau_1)}. \tag{2.16}$$

Then applying boundary conditions (2.8) and (2.9), we have, respectively,

$$\lambda^f(\tau_1) = \frac{f(\tau_0)}{\frac{\partial T}{\partial \mathbf{n}}(\tau_0)} \frac{c(\tau_1) d\sigma(\tau_0)}{c(\tau_0) d\sigma(\tau_1)},$$
$$\lambda^1(\tau_1) = \frac{1}{\frac{\partial T}{\partial \mathbf{n}}(\tau_0)} \frac{c(\tau_1) d\sigma(\tau_0)}{c(\tau_0) d\sigma(\tau_1)},$$

so that we have by formula (2.10) of β,

$$\beta(\tau_1) = \frac{\lambda^f(\tau_1)}{\lambda^1(\tau_1)} = f(\tau_0). \tag{2.17}$$

We see that, along the ray, $\beta(\tau_1) = \frac{\lambda^f(\tau_1)}{\lambda^1(\tau_1)}$ is nonsingular and uniformly distributes the traveltime residual $f(\tau_0)$, which exactly serves our purpose to remove the singularity of the adjoint-state field. The above argument justifies formula (2.10). ∎

In general, in a generic medium, there exist multiple rays connecting the source $\mathbf{x}_s$ to an arbitrary point $\mathbf{x}$ [48]. However, the concept of viscosity solution for the eikonal equation [9] singles out a unique ray to connect the source to the point $\mathbf{x}$ among all possible rays, except those points $\mathbf{x}$ in a set of measure zero. However, a monotone scheme [10] designed to compute such a viscosity solution will limit the influence of the measure-zero set to a set of measure zero. Accordingly, since the adjoint-state equation uses the gradient of ∇T (defining the ray direction) as the advection coefficient, the influence of the measure-zero set will be restricted to a measure-zero set as well. Therefore, we will apply formula (2.10) globally in the sense of viscosity solution.

Therefore, instead of the original $\tilde{c} = -\lambda/c^3$, we will take

$$\tilde{c} = -\frac{\lambda^f}{\lambda^1}\frac{1}{c^3} = -\frac{\beta(\mathbf{x})}{c^3} \tag{2.18}$$

as the gradient descent direction to minimize the energy.

2.2.1. An illustrative example. We use an example to illustrate this point further. We consider the eikonal equation on a unit sphere $D = B(\mathbf{0}, 1)$ in the two- or three-dimensional space, where $d = 2, 3$:

$$|\nabla T| = s_0 \qquad \text{on} \qquad D \setminus \{\mathbf{0}\}, \tag{2.19}$$
$$T|_{\mathbf{x}=\mathbf{0}} = 0, \tag{2.20}$$

where the slowness s_0 is constant.

We need to solve the following adjoint state equation after solving the eikonal equation:

$$-\nabla \cdot (\lambda \nabla T) = 0, \tag{2.21}$$

$$\frac{\partial T}{\partial \mathbf{n}} \lambda|_{\partial D} = f, \tag{2.22}$$

where f is the traveltime residual, and $\partial D = \partial B(\mathbf{0}, 1)$. We denote λ^f the solution of this equation.

To normalize the singular behavior of the adjoint state, we solve the adjoint state equation (2.21) once more with a different boundary condition,

$$\frac{\partial T}{\partial \mathbf{n}} \lambda|_{\partial D} = 1, \tag{2.23}$$

and we denote the resulting solution to be λ^1. It is easy to check that

$$\lambda^1 = \frac{1}{s_0 |\mathbf{x}|^{d-1}}, \tag{2.24}$$

which is singular at the source (the origin).

Next we normalize λ^f by λ^1 so that we have a new function

$$\beta(\mathbf{x}) = \frac{\lambda^f(\mathbf{x})}{\lambda^1(\mathbf{x})}, \tag{2.25}$$

which is nonsingular, as we have shown that

$$\beta(\mathbf{x}) = f\left(\frac{\mathbf{x}}{|\mathbf{x}|}\right). \tag{2.26}$$

2.3. Multiple point sources. In the above calculation, we use the first-arrivals at different receivers associated with a single point source. If we perform multiple such experiments, namely, we have many such data sets, then those can be easily incorporated into the formulation. For example, we can assume that there are N point sources located at $\mathbf{x}_s^i$, for $i = 1, \ldots, N$, and N sets of first-arrival travel-time measurements T_i^* associated with these N sources are available. Then we can simply define a new energy

$$E^N(c) = \frac{1}{2} \sum_{i=1}^{N} \int_{\partial \Omega_p} |T_i - T_i^*|^2 ,$$

where T_i is the solution from the eikonal equation with the corresponding point source condition $T(\mathbf{x}_s^i) = 0$. Utilizing the same approach as above, we have the following perturbation in the energy:

$$\frac{\delta E^N}{\epsilon} = \int_{\Omega_p} \frac{\tilde{c}}{c^3} \sum_{i=1}^{N} \lambda_i ,$$

where λ_i is the adjoint variable of T_i satisfying $-\nabla \cdot (\lambda \nabla T) = 0$ with the boundary condition, $(\mathbf{n} \cdot \nabla T_i)\lambda_i = T_i^* - T_i$ for $i = 1, \ldots, N$.

Consequently, after normalization, we can choose the following gradient direction to minimize the energy $E^N(c)$:

$$\tilde{c} = -(I - \nu \Delta)^{-1} \left(\frac{1}{c^3} \sum_{i=1}^{N} \beta_i \right) ,$$

where $\beta_i = \lambda_i^f / \lambda_i^1$.

2.4. Mismatch functional based on the L^1 norm. Other mismatch functionals are also possible. A popular choice is the L^1 mismatch functional widely used in various applications from image processing, to high dimensional data processing, to sparse signal recovery.

Mathematically, one replaces the L^2 least-squares problem by the L^1 mismatch between the measurements and the synthetic data obtained from the model, i.e.,

$$E(c) = \int_{\partial\Omega_p} |T - T^*| d\Gamma \,. \tag{2.27}$$

Following a similar derivation as in the least-squares functional, we obtain the same adjoint state equation but with a different boundary condition given by

$$(\mathbf{n} \cdot \nabla T)\lambda = \operatorname{sgn}(T^* - T) \,, \tag{2.28}$$

where $\operatorname{sgn}(\cdot)$ is the signum function that is approximated by $\operatorname{sgn}(x) = x/\sqrt{x^2 + \epsilon^2}$ for some parameter $\epsilon > 0$ to avoid division-by-zero.

Other needed ingredients are similar to the case in the L^2 least-squares sense.

3. Algorithm and numerical implementations. In this section, we first summarize the overall algorithm for solving the inverse problem. Then we will give numerical details for each step of the algorithm.

3.1. Tomography algorithm. Here we first summarize the algorithm in Algorithm 3.1 for solving this tomography problem in irregular domains.

Algorithm 3.1 Tomography algorithm.

Input: The source location (x_s, z_s) and convergence parameters δ and $k_{\max}$.
Output: $T_{i,j}$ in $\Omega_p \cup \Omega_e$.
Initialization: obtain c^0 by solving $(I - \nu\Delta)c^0 = 0$ with the boundary condition $c^0|_{\partial\Omega_p} = c_{\text{exact}}|_{\partial\Omega_p}$.
While $||\tilde{c}^k(x,z)||_2 > \delta$ and $k < k_{\max}$ **do**
Obtain $T(x,z)$ by solving (2.1) with the point source condition (2.2) using $c = c^k$;
Obtain $\lambda^f(x,z)$ and $\lambda^1(x,z)$ by solving (2.4) with the boundary condition (2.5) and (2.9);
Construct $\lambda(x,z) = \lambda^f(x,z)/\lambda^1(x,z)$;
Obtain $\tilde{c}^k$ using (2.6);
Determine ϵ^k using, for example, the Armijo–Goldstein rule or simply $\epsilon^k = \epsilon$;
Update $c^{k+1} = c^k + \epsilon^k \tilde{c}^k$;
Update $k \leftarrow k + 1$.
End while.

To start the iteration, we need to initialize c^0. Here in the algorithm, we assume that we know the velocity at receivers, giving $c^0|_{\partial\Omega_p} = c_{\text{exact}}|_{\partial\Omega_p}$. This condition can be replaced by other assumptions. In practice, due to the nonlinearity of the problem, different initial guesses will generally converge to different energy minimizers. This nonuniqueness can be overcome by some a priori knowledge of the model.

3.2. Extension to Ω_e. Because of the domain being irregular, there are two main numerical issues in implementing the above algorithm. The *first* one is how to solve the eikonal equation in an irregular domain. The *second* one is how to impose the boundary condition (2.5) on $\partial\Omega_p$ so that the mismatch information can be back-propagated into the interior. These two issues are in general challenging tasks for

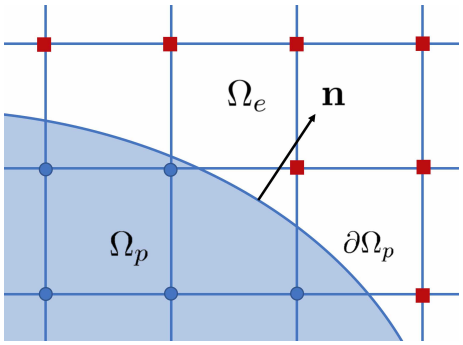

FIG. 2. *Extension to* Ω_e.

standard finite-difference methods. In this work, we propose to apply the level-set method to handle these difficulties in an irregular domain.

The first step is to embed the domain Ω_p into a rectangular domain $\Omega_p \cup \Omega_e$ so that computations can be done in a rather straightforward way; see Figure 1. We introduce a level set function ϕ with $\phi(\mathbf{x}) < 0$ if $\mathbf{x} \in \Omega_p$ and $\phi(\mathbf{x}) > 0$ if $\mathbf{x} \in \Omega_e$ such that the boundary of Ω_p is represented implicitly by the zero level set. Then we follow the standard level-set approach to extend the traveltime function T from Ω_p to Ω_e so that the function is constant in the normal direction from $\partial\Omega_p$. Mathematically, this orthogonal extension idea can be achieved by extending the outward normal vector $\mathbf{n}$ defined on $\partial\Omega_p$ using the level-set function which is defined everywhere so that $\mathbf{n}(\mathbf{x}) = \nabla\phi/\|\nabla\phi\|$ is now defined everywhere in the rectangular domain.

Then, we solve the extension equation

$$\mathbf{n} \cdot \nabla T = 0 \text{ for } x \in \Omega_e \tag{3.1}$$

for T, where $\mathbf{n} = \nabla\phi/\|\nabla\phi\|$ and the boundary condition $T_{\partial\Omega_p}$ is given by the solution to the eikonal equation; see Figure 2. This extension equation is a hyperbolic PDE with characteristics following the normals of contours of the level-set function, namely, $\mathbf{n}$. Since $\phi < 0$ in Ω_p and $\mathbf{n}$ is a vector field pointing away from the boundary defined by $\{\mathbf{x} : \phi(\mathbf{x}) = 0\}$, the equation enforces that the traveltime function T is constant along the characteristics and the information will be propagated from the boundary $\partial\Omega_p$ outward to Ω_e.

As a side remark, we may try to first extend the velocity field c (instead of the traveltime T) from Ω_p to Ω_e by solving $\mathbf{n} \cdot \nabla c = 0$, followed by the eikonal equation in the whole rectangular domain. However, in this case, there is no control in the causality and the characteristics might first leave the domain and come back later. This might lead to a wrong causality and further lead to a wrong solution.

3.3. A fast sweeping method for eikonal in Ω_p and extension in Ω_e. The fast sweeping method was originated in Boue and Dupis [4], and its first PDE formulation was used in implicit and nonparametric shape reconstruction from unorganized points [51]; Zhao [52] proved the $O(N)$ convergence of the method for the eikonal equation with constant speed based on the Godunov Hamiltonian on Cartesian meshes; later on, the fast sweeping method was extended to treat Hamilton–Jacobi equations with convex Hamiltonians based on the Godunov numerical Hamiltonian [45] and to handle Hamilton–Jacobi equations with nonconvex Hamiltonians based on the Lax–Friedrichs numerical Hamiltonian [16]; see [45, 16] and references therein for

the fast sweeping method on Cartesian meshes and [33] for the method on triangulated meshes.

To be self-contained, we give a short summary of the fast sweeping method for eikonal equations. To avoid cluttered notation we present the algorithm for the two-dimensional case only; see [52] for more details. First we discretize the rectangular domain $\Omega \subset \mathcal{R}^2$ into a uniform mesh with mesh points $\mathbf{x}_{i,j}$ and mesh sizes $\Delta x = \Delta z = h$, and we denote the numerical solution at $\mathbf{x}_{i,j}$ by $T_{i,j}$. The mesh size is assumed to be small enough to resolve the geometry and the regularity of the boundary $\partial\Omega_p$. In particular, we require that the mesh size is smaller than the reciprocal of the largest curvature along the boundary so that the grid has enough resolution to reasonably approximate the $\partial\Omega_p$. In most of the applications discussed in this work, on the other hand, we are looking at a circular region. This consideration of the boundary resolution does not have a significant impact on how to decide the computational mesh.

Applying the Godunov numerical Hamiltonian to the eikonal equation, for $i = 2, \ldots, I-1$, $j = 2, \ldots, J-1$, we have

$$[(T_{i,j} - T_{xmin})^+]^2 + [(T_{i,j} - T_{zmin})^+]^2 = \frac{h^2}{c_{i,j}^2}, \tag{3.2}$$

where $T_{xmin} = \min(T_{i-1,j}, T_{i+1,j})$, $T_{zmin} = \min(T_{i,j-1}, T_{i,j+1})$, and $(x)^+$ denotes the positive part of x. At the boundary of the computational domain one-sided difference is used.

When solving the extension equations $\mathbf{n} \cdot \nabla T = (p, q) \cdot (T_x, T_z) = 0$, we follow the ideas in [19, 22, 23] to develop a simple upwind differencing to discretize the equation and derive the update formulas accordingly. At each point $(x_i, z_j) \in \Omega_e$, we define $p^{\pm} = \frac{1}{2}(p_{i,j} \pm |p_{i,j}|)$ and, therefore, obtain the update formula given by

$$T_{i,j} \leftarrow \frac{p^+ T_{i-1,j} - p^- T_{i+1,j} + q^+ T_{i,j-1} - q^- T_{i,j+1}}{|p_{i,j}| + |q_{i,j}|}. \tag{3.3}$$

A straightforward implementation consists of two stages: at the first stage, we obtain the solution to the eikonal equation in Ω_p without any modification to grid points in Ω_e; at the second stage, we sweep through the grid points in Ω_e to update the traveltime value by (3.3).

For ease of implementation, typical fast sweeping methods on Cartesian meshes sweep through the structured grid points for each of total 2^d orderings, where d represents the dimension of the computational space. Therefore, when implementing the first stage of the above approach, one is required to set a logic check to decide if the grid point is located inside Ω_p. If the check is false, the code does not update any grid value. Similarly, the code updates any grid value only if it is located inside Ω_e at the second stage of the algorithm. This code is therefore less compact and might seem to be computationally less efficient. Another possibility is to combine these two iterative schemes by following a similar approach as in [49] for solving the surface eikonal equation. The idea is to combine two stages into one so that one updates the grid value depending on the logic statement if the location is inside Ω_p or not. Mathematically, one incorporates this idea into an iterative formulation to obtain the following algorithm:

$$T_{i,j} \leftarrow \begin{cases} \dfrac{p^+ T_{i-1,j} - p^- T_{i+1,j} + q^+ T_{i,j-1} - q^- T_{i,j+1}}{|p_{i,j}| + |q_{i,j}|} & \text{if } (x_i, z_j) \in \Omega_e, \\ \min(T^x_{\min}, T^z_{\min}) + \Delta x / c_{i,j} & \text{if } (x_i, z_j) \in \Omega_p \text{ and } |T^x_{\min} - T^z_{\min}| > \Delta x / c_{i,j}, \\ \dfrac{1}{2}\left[T^x_{\min} + T^z_{\min} + \sqrt{2\Delta x^2 / c_{i,j}^2 - (T^x_{\min} - T^z_{\min})^2}\right] & \text{if } (x_i, z_j) \in \Omega_p \\ \textit{and } |T^x_{\min} - T^z_{\min}| \le \Delta x / c_{i,j}. \end{cases} \tag{3.4}$$

Algorithm 3.2 A fast sweeping method for coupling the eikonal equation in Ω_p and the extension equation in Ω_e.

Input: The source location (x_s, z_s), the mesh size Δx, and the level set representation of the surface $\phi_{i,j}$.
Output: $T_{i,j}$ in $\Omega_p \cup \Omega_e$.
Initialization: Set $T_{i,j} = 0$ if (x_i, z_j) is at the point source, otherwise $T_{i,j} = \infty$.
While not converge **do**
  For each of the four sweeping directions
    If $\phi_{i,j} \le 0$ and $T_{i,j} \neq 0$,
      update $T_{i,j}$ using (3.2);
    else if $\phi_{i,j} > 0$
      update $T_{i,j}$ using (3.3) with $\mathbf{v} = (p, q) = \mathrm{sgn}(\phi)\mathbf{n}$.
    end If
  end For
end While

The algorithm is given in Algorithm 3.2.

This Godunov fast sweeping method for the eikonal equation and the extension equation is computationally efficient. Since the numerical scheme follows the causality, the overall computational complexity is given by $O(N)$, where N is the total numerical of grid points in the rectangular domain $\Omega_p \cup \Omega_e$.

3.4. A fast sweeping method for the adjoint state in Ω_p. Next we design a fast sweeping method for the adjoint-state equation (2.4). Once again to simplify notation, we give a two-dimensional formulation only; the extension to a three-dimensional formulation is straightforward. The adjoint-state equation (2.4) can be written in the following form:

$$(a\lambda)_x + (b\lambda)_z = 0\,,$$

where a and b are given functions of (x, z). Considering a computational cell centered at (x_i, z_j) and discretizing the equation in conservation form, we have

$$\frac{1}{\Delta x}\left(a_{i+1/2,j}\lambda_{i+1/2,j} - a_{i-1/2,j}\lambda_{i-1/2,j}\right) + \frac{1}{\Delta z}\left(b_{i,j+1/2}\lambda_{i,j+1/2} - b_{i,j-1/2}\lambda_{i,j-1/2}\right) = 0\,.$$

The values of λ on the interfaces, $\lambda_{i\pm1/2,j}$ and $\lambda_{i,j\pm1/2}$, are determined according to the propagation of characteristics. In the case when $a_{i+1/2,j} > 0$, the characteristic for determining λ goes from the left-hand side of the interface to the right-hand side, and this suggests that we use the value $\lambda_{i,j}$ to define $\lambda_{i+1/2,j}$; otherwise, we have $\lambda_{i+1/2,j} = \lambda_{i+1,j}$. The terms $\lambda_{i,j\pm1/2}$ can be defined in a similar way. Introducing the notation

$$a^{\pm}_{i+1/2,j} = \frac{a_{i+1/2,j} \pm |a_{i+1/2,j}|}{2} \quad , \quad a^{\pm}_{i-1/2,j} = \frac{a_{i-1/2,j} \pm |a_{i-1/2,j}|}{2}\,,$$
$$b^{\pm}_{i,j+1/2} = \frac{b_{i,j+1/2} \pm |b_{i,j+1/2}|}{2} \text{ and } b^{\pm}_{i,j-1/2} = \frac{b_{i,j-1/2} \pm |b_{i,j-1/2}|}{2}\,,$$

we have

$$\frac{1}{\Delta x}\left[(a^+_{i+1/2,j}\lambda_{i,j} + a^-_{i+1/2,j}\lambda_{i+1,j}) - (a^+_{i-1/2,j}\lambda_{i-1,j} + a^-_{i-1/2,j}\lambda_{i,j})\right]$$
$$+\frac{1}{\Delta z}\left[(b^+_{i,j+1/2}\lambda_{i,j} - b^-_{i,j+1/2}\lambda_{i,j+1}) - (b^+_{i,j-1/2}\lambda_{i,j-1} - b^-_{i,j-1/2}\lambda_{i,j})\right] = 0\,,$$

which can be rewritten as

$$\lambda_{i,j} = \left(\frac{a^+_{i+1/2,j} - a^-_{i-1/2,j}}{\Delta x} + \frac{b^+_{i,j+1/2} - b^-_{i,j-1/2}}{\Delta z}\right)^{-1}$$
$$\times\left(\frac{a^+_{i-1/2,j}\lambda_{i-1,j} - a^-_{i+1/2,j}\lambda_{i+1,j}}{\Delta x} + \frac{b^+_{i,j-1/2}\lambda_{i,j-1} - b^-_{i,j+1/2}\lambda_{i,j+1}}{\Delta z}\right). \tag{3.5}$$

This gives an expression to build up a fast sweeping-type iterative method.

To apply this iterative scheme to (2.4), we need to specify the function values of a and b not at the cell centers (x_i, z_j) but on the cell interfaces $(x_{i\pm1/2}, z_j)$ and $(x_i, z_{j\pm1/2})$. This can be done easily using central differences. For example, we have $a_{i+1/2,j} = -(T_{i+1,j} - T_{i,j})/\Delta x$ and $a_{i-1/2,j} = -(T_{i,j} - T_{i-1,j})/\Delta x$. In addition, we have to incorporate the boundary condition (2.5) into the above linear system for λ as well. Then we can show that the coefficient matrix of the resulting linear system for λ is irreducibly diagonally dominant, and therefore the alternating symmetrical Gauss–Seidel iteration converges.

For grid points in Ω_e, we simply assign the value $\lambda_{i,j}$ based on the boundary condition given by (2.5). While the right-hand side of the expression is already defined according to Algorithm 3.2, we have to pay attention to the coefficient in front of λ in the expression. The quantity $\mathbf{n}\cdot\nabla T$ is actually computed in the previous algorithm by assigning $\mathbf{n}\cdot\nabla T = 0$ which, unfortunately, cannot be used in detemining the boundary condition. We here propose the following approach to extend the quantity from the interior Ω_p to the boundary so that it can be used in the boundary condition. To simplify notation, we first introduce $U(\mathbf{x}) = \mathbf{n}\cdot\nabla T$ for $\mathbf{x}\in\Omega_p$. Now, we extend this quantity to the exterior by solving the extension equation $\mathbf{n}\cdot\nabla U = 0$ in Ω_e using the fast sweeping method. Once the iteration converges, we assign $\lambda_{i,j} = \left(T^*_{i,j} - T_{i,j}\right)/U_{i,j}$, which is the needed boundary condition.

Algorithm 3.3 A fast sweeping algorithm for (2.4) and (2.5).

Input: The mesh size Δx, the level set representation of the surface $\phi_{i,j}$, and a convergence criterion $\epsilon > 0$.
Output: $\lambda_{i,j}$ in Ω_p.
Initialization: Set $\lambda_{i,j} = 0$ in Ω_p.
Compute $U = \mathbf{n}\cdot\nabla T$ in Ω_p.
Solve $\mathbf{n}\cdot\nabla U = 0$ for U in Ω_e and assign $\lambda = (T^* - T)/U$.
While $||\lambda^{n+1} - \lambda^n||_{L^1} \le \epsilon$ **do**
  For each of the four sweeping directions
    If $\phi_{i,j} \le 0$
      update $\lambda_{i,j}$ using (3.5);
    end If
  end For
end While

This fast sweeping method for hyperbolic conservation laws in Ω_p has been proposed in [19]. A more general formulation based on the Lax–Friedrichs flux has been recently discussed in [6]. Although there is no theoretical convergence proof available, we have observed that the numerical scheme converges in a handful of iterations (for example, two or three iterations for the sinusoidal model) in our numerical tests.

3.5. Regularization of $\tilde{c}^k$ in irregular domains. To update the velocity, we regularize the perturbation by the same elliptic operator $(I - \nu\Delta)$ in the bounded irregular domain Ω_p with the zero Dirichlet boundary condition.

The idea to discretize the Laplacian is to follow the approach described in [5] for solving the Stefan problem for crystal growth simulation. The first step is to classify grid points in Ω_p into two groups. The first group consists of mesh points where all four immediate neighbors stay inside Ω_p, and the rest of the mesh points define the second group. For those points in the first group, one can follow the usual five-point finite difference to approximate the Laplacian. For the second group, one imposes the Dirichlet boundary condition by extrapolating the solution from Ω_p to Ω_e. In particular, consider the one-dimensional case and assume that $\phi_i \cdot \phi_{i+1} < 0$ so that $x_i \in \Omega_p$ and $x_{i+1} \in \Omega_e$. Using linear extrapolation, we enforce $\tilde{c} = 0$ at $\phi = 0$ and obtain $\tilde{c}^*_{i+1} = \tilde{c}_i\, \phi_{i+1}/\phi_i$. Then we substitute this in the approximation of the Laplacian at $x = x_i$, i.e.,

$$\left.\frac{\partial^2 \tilde{c}}{\partial x^2}\right|_{x=x_i} = \frac{\tilde{c}_{i-1} - 2\tilde{c}_i + \tilde{c}^*_{i+1}}{\Delta x^2}\,.$$

3.6. Partial measurements. In all discussions above, we have assumed that full measurements are provided on the boundary $\partial\Omega_p$ whenever it is necessary in various parts of the overall algorithm. In this section, we consider a simple approach to relax such a condition. Following the approaches proposed in [18, 19, 20], we denote Γ the set of locations where measurements are provided. The least-squares mismatch functional (2.3) can, therefore, be replaced by

$$E(c) = \frac{1}{2}\int_{\partial\Omega_p} |T - T^*|^2 \delta(\Gamma) d\Gamma\,, \tag{3.6}$$

where $\delta(\cdot)$ is the Dirac's delta function. The adjoint state equation to be solved will be kept unchanged. The corresponding change in the implementation will be on the right-hand side of the boundary condition (2.5). Instead of having $(T^* - T)$ on the boundary $\partial\Omega_p$, we now have $(T^* - T)\delta(\Gamma)$ so that the contribution from the mismatch comes solely at the locations where we have the measurement, while the boundary condition is zero when we do not have any information. Numerically, one can simply regularize the delta function for ease of implementation using the finite-difference approaches.

4. Numerical examples. In this section, we consider several two- and three-dimensional examples to demonstrate effectiveness and robustness of the algorithm. We will also compare the adjoint variables constructed by the original formulation in [19] and the proposed normalization approach. One can then observe that such a simple normalization approach can effectively remove the singularity at the point source. We are also going to test the algorithm on a synthetic dataset from an ultrasound CT experiment.

For all the examples, unless otherwise stated, we use the normalized adjoint-state solution to update the velocity.

4.1. A constant model. In this example, we consider the constant model where the true velocity is given by the constant $c(x,z) = 1$. The domain Ω_p is a disk of radius $r = 0.75$, while all computations are done on an underlying Cartesian mesh of size 129×129 in the domain $[-1,1]^2$. We locate 20 point sources uniformly near the boundary of the circular domain. Measurements are given on $\partial\Omega_p$ whenever necessary.

We have chosen two different initial guesses to demonstrate the performance of the algorithm. In Figure 3, we consider the initial guess $c^0 = 1.75 - \sqrt{x^2+y^2}$ so that it matches with the exact velocity on the boundary of Ω_p. However, since the initial guess contains a singularity at the origin, our method has difficulty in converging to the exact solution since the perturbation at each iteration is a smooth function. In Figure 4, we replace the singular initial guess by a smooth function $c^0 = 1 + 0.1\cos(\pi\sqrt{x^2+y^2}/1.5)$. Our approach converges to the exact solution nicely with an error of $O(10^{-4})$.

We have also looked into the construction of the velocity perturbation in Figure 5 based on the proposed algorithm to remove the singularity in the adjoint state. For each of the sources, we have an adjoint variable by solving the adjoint equation. In Figure 5(a), we have plotted the adjoint variable associated with the first, the eighth, and the fifteenth source at the first iteration. As the misfit along the boundary

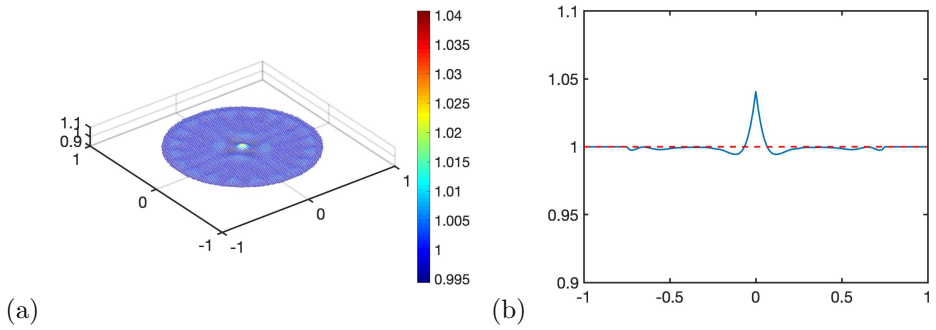

FIG. 3. *Example* 4.1. *Twenty sources are located uniformly on a circle of radius* 0.7 *with the initial condition given by* $c^0 = 1.75 - \sqrt{x^2+y^2}$. (a) *The inverted velocity.* (b) *The cross section of the solution along* $x = 0$. *The inverted solution is plotted in a blue solid line, while the exact solution is shown in a red dashed line.*

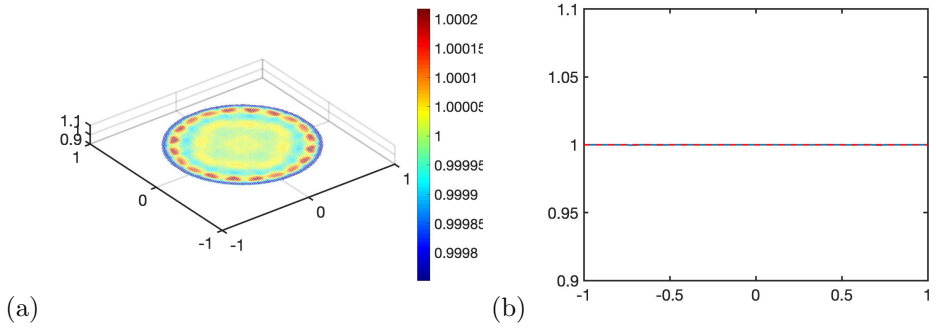

FIG. 4. *Example* 4.1. *Twenty sources are located uniformly on a circle of radius* 0.7 *with the initial condition given by* $c^0 = 1 + 0.1\cos(\pi\sqrt{x^2+y^2}/1.5)$. (a) *The inverted velocity.* (b) *The cross section of the solution along* $x = 0$. *The inverted solution is plotted in a blue solid line, while the exact solution is shown in a red dashed line.*

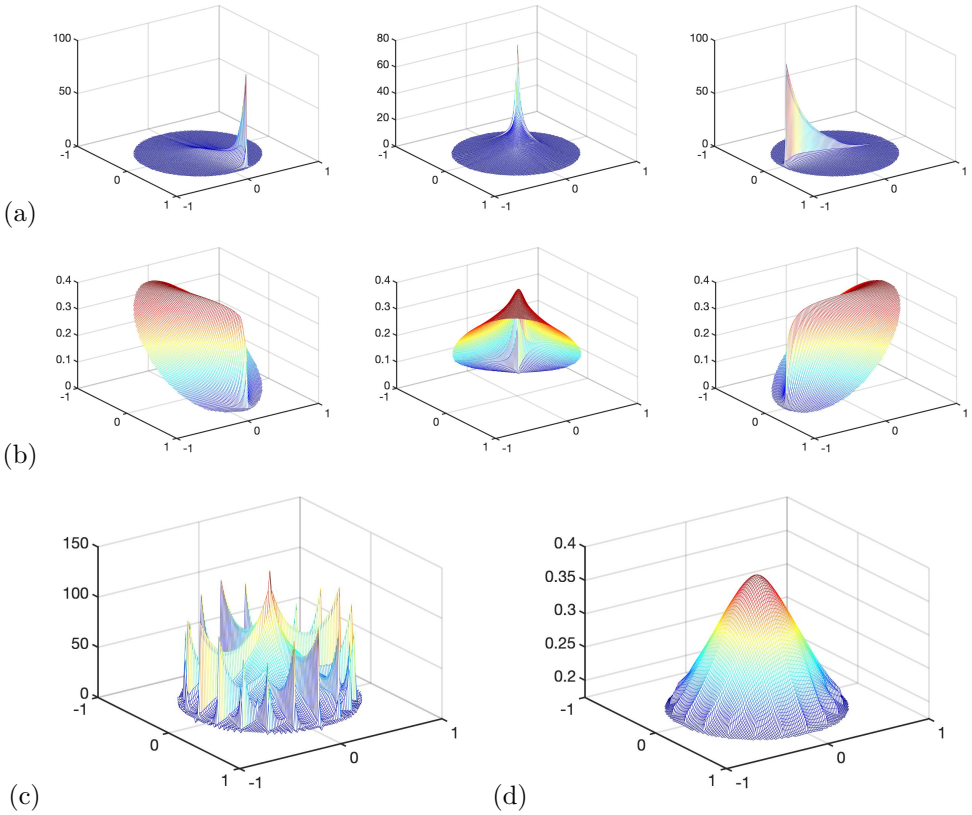

FIG. 5. *Example* 4.1. *The adjoint variables in the first iteration.* (a) *The original adjoint variable for the perturbation associated to the first, eighth, and fifteenth sources.* (b) *The proposed normalized adjoint variable associated to the first, eighth and fifteenth sources.* (c) *The sum of the original adjoint solution from all sources.* (d) *The sum of the proposed adjoint solution from all sources.*

propagates backward toward the source, we can see that the solution develops a singularity and blows up at the corresponding source location. Therefore, using the original approach, the sum of these adjoint variables will lead to an undesired perturbation as shown in Figure 5(c). This requires us to impose rather strong Tikhonov regularization when updating the velocity. On the other hand, the normalization approach allows us to obtain both a much more regular adjoint variable associated with each individual point source as shown in Figure 5(b) and a much more regular sum of the adjoint variables as shown in Figure 5(d).

4.2. A Gaussian model. In this example, we consider the Gaussian model [18, 19, 12] given by

$$c(x,y) = 3 - \frac{1}{2}\exp\left(-\frac{x^2+(y+0.5)^2}{0.5^2}\right) - \exp\left(-\frac{x^2+(y-0.25)^2}{0.5^2}\right).$$

We use the same domain Ω_p as in section 4.1. We also discretize the computational domain $[-1,1]^2$ using the same number of mesh points.

We investigate the robustness of the proposed algorithm to noise in measurements. Figure 6 shows the inverted solutions and their cross sections when measurements on

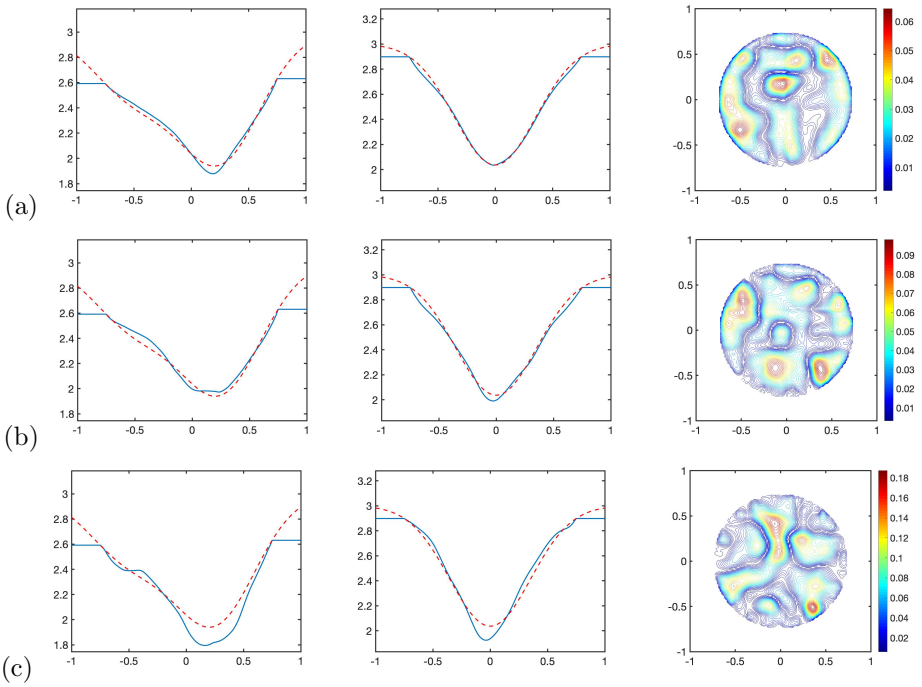

FIG. 6. *Example* 4.2. *Measurements with noise. Twenty sources are located uniformly on a circle of radius* 0.7. (a) *We invert for the velocity using measurements with* 5% *Gaussian noise. From left to right: The cross section of the solution along* $x = 0$ *and along* $y = 0$*, and also the contour plot of the absolute error in the solution.* (b)–(c) *We invert for the velocity using measurements with* (b) 10% *and* (c) 20% *Gaussian noise.*

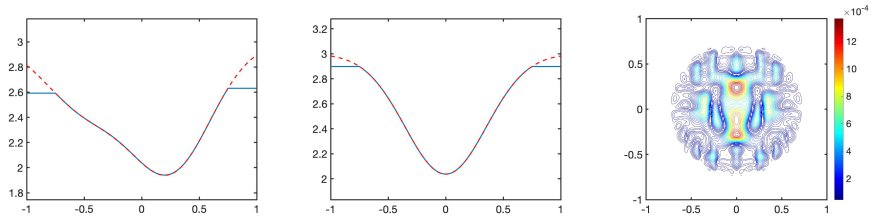

FIG. 7. *Example* 4.2. L_1 *mismatch functional. Twenty sources are located uniformly on a circle of radius* 0.7. *From left to right: The cross sections of the inverted velocity along* $x = 0$ *and along* $y = 0$*, and the contour plot of the absolute error in the solution.*

the boundary $\partial\Omega_p$ are added with 5%, 10%, and 20% Gaussian noise. When the noise level is relatively low, such as 5%, as shown in Figure 6(a), the obtained solution seems to be mildly degraded with the maximum relative error (defined in a pointwise fashion given by $|c - c^{\infty}|/c$) increased to approximately from 0.01 (for the noiseless case we have tested) to 0.035 as shown in Figure 6(a). When we double the amount of noise in the measurements, the maximum relative errors increase correspondingly as shown in Figures 6(b) and (c). Nevertheless, the solutions still match reasonably well with the exact velocity model.

As discussed earlier, one can easily replace the least-squares mismatch by other functions. Figure 7 shows the inverted velocity based on the L_1 mismatch (2.27) with

clean measurements. We show the cross sections of the solution along both the line $x = 0$ and the line $y = 0$, and also the contour plots of the absolute error. We find that our inverted velocity based on the L_1 functional matches well with the exact solution with quality similar to the one obtained by the least-squares mismatch function (2.3).

4.3. A sinusoidal model. Here we consider the following sinusoidal model used in [42, 12]:

$$c(x, y) = 1 + 0.2 \sin\left[\frac{\pi}{2}(y + 1)\right] \sin\left[3\pi(x + 0.55)\right] .$$

This is a challenging example since the velocity model has relatively large variations to cause a lot of caustics. The computational setup is the same as that in section 4.1. The solution from the data set of 20 sources is shown in Figure 8. The maximum absolute error is around 0.01 near the center of the computational domain far away from the location of the receivers. Figure 9 shows the solution to the adjoint state equation associated to several sources in the first iteration. Similar to what we have observed in the constant model case in section 4.1, the solution develops singularity at the corresponding source location. With the proposed normalization approach, we can remove the singularities in the adjoint variables, as shown in Figure 9(d).

In all examples above, we have assumed that we can obtain full and complete measurements on $\partial\Omega_p$. In Figure 10, on the other hand, we assume that we are provided with measurements on only certain parts of the boundary.

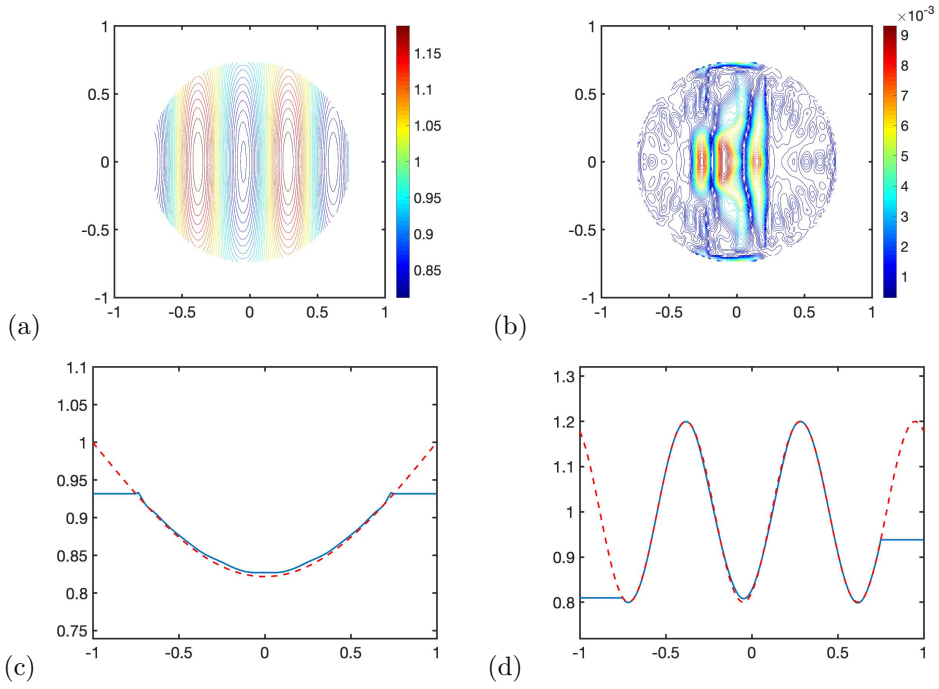

FIG. 8. *Example* 4.3. *Circular domain. Twenty sources are located uniformly on a circle of radius* 0.7. (a) *The final inverted velocity.* (b) *The contour plot of the absolute error in the solution.* (c) *The cross section of the solution along* $x = 0$. *The inverted solution is plotted in a blue solid line, while the exact solution is shown in a red dashed line.* (d) *The cross section of the solution along* $y = 0$.

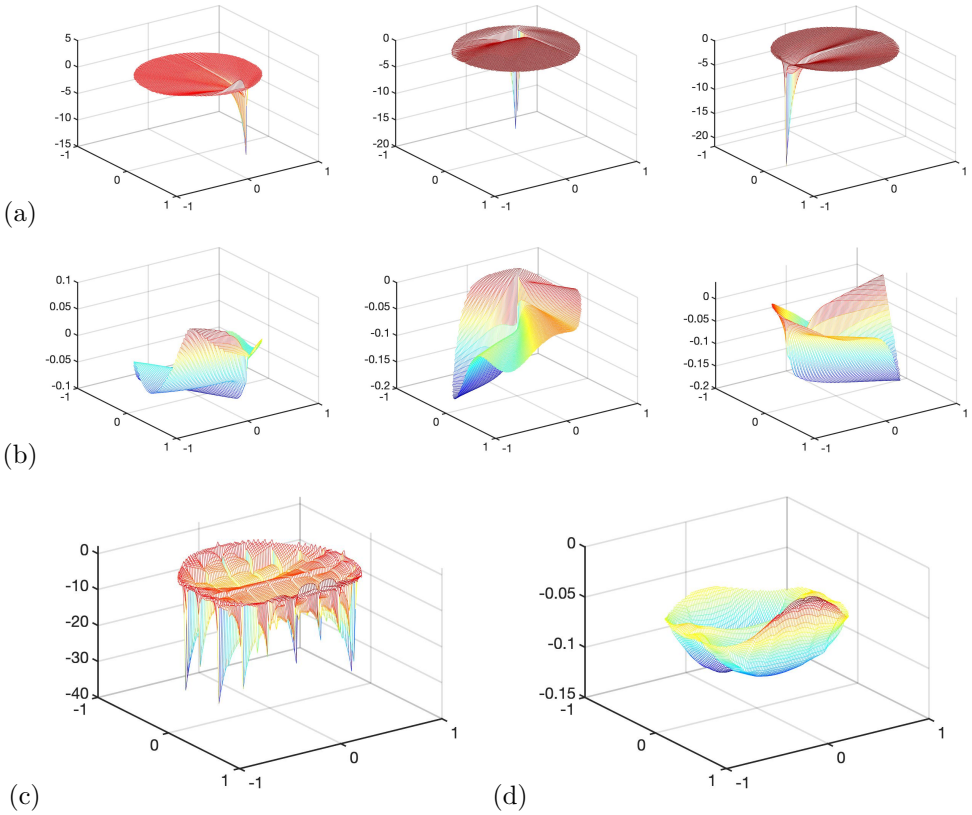

FIG. 9. *Example* 4.3. *The adjoint variables in the first iteration.* (a) *The original adjoint variable for the perturbation associated to the first, eighth, and fifteenth sources.* (b) *The proposed normalized adjoint solution associated to the first, eighth, and fifteenth sources.* (c) *The sum of the original adjoint variables from all sources.* (d) *The sum of the proposed normalized adjoint variables from all sources.*

In Figure 10(a), we keep 20 uniformly located point sources on $r = 0.7$ but carry out measurements only on a part of the boundary $\partial\Omega_p$, which is specified by $|x| > 0.65$, i.e.,

$$\partial\Omega_p^{(a)} = \{(r,\theta) : r = 0.75, \theta \in [-\theta^*, \theta^*] \cup [\pi - \theta^*, \pi + \theta^*]\},$$

where $\theta^* = \cos^{-1}\left(\frac{65}{75}\right)$.

In Figure 10(b), we carry out measurements only on a part of the boundary $\partial\Omega_p$ which is specified by $|y| > 0.65$, i.e.,

$$\partial\Omega_p^{(b)} = \left\{(r,\theta) : r = 0.75, \theta \in \left[\frac{\pi}{2} - \theta^*, \frac{\pi}{2} + \theta^*\right] \cup \left[\frac{3\pi}{2} - \theta^*, \frac{3\pi}{2} + \theta^*\right]\right\}.$$

The accuracy in the inversion is dropped significantly compared to the full measurements as shown in Figure 8.

Figure 11 shows the inverted velocity obtained by replacing the least-squares functional with the L_1 functional (2.27) with clean measurements. The inverted solution also matches well with the exact solution. To demonstrate the effect of the proposed normalization approach for the adjoint variable, we show the sum of all the original adjoint variables from each individual source and the sum of all the normalized adjoint variables from all sources in Figure 12. Similar to the least-squares

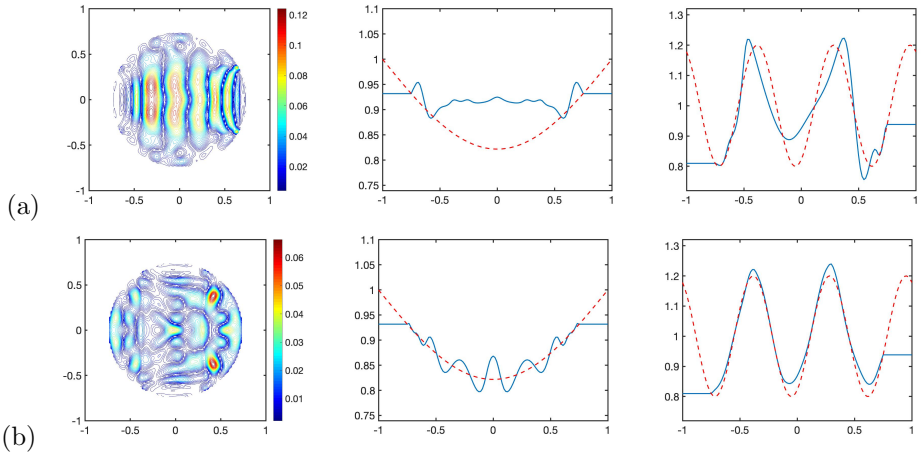

FIG. 10. *Example* 4.3. *Partial measurements on a circular domain. Twenty sources are located uniformly on a circle of radius* 0.7. (a) *The error in the inverted velocity with measurements given along the two arcs* $|x| > 0.65$ *defined by* $\partial\Omega_p^{(a)}$. *The cross section of the solution along* $x = 0$ *and* $y = 0$. (b) *The error in the inverted velocity with measurements given along the two arcs* $|y| > 0.65$ *defined by* $\partial\Omega_p^{(b)}$. *The cross sections of the solution along* $x = 0$ *and* $y = 0$.

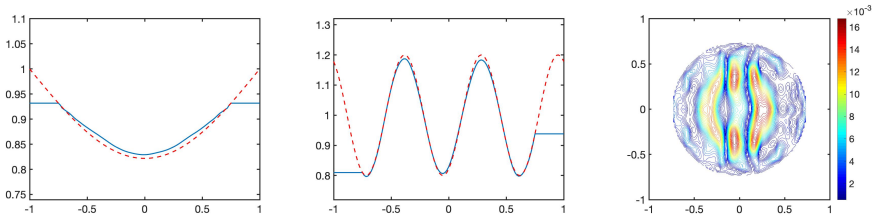

FIG. 11. *Example* 4.3. L_1 *mismatch functional. Twenty sources are located uniformly on a circle of radius* 0.7. *From left to right: The cross sections of the inverted velocity along* $x = 0$ *and along* $y = 0$, *and the contour plot of the absolute error in the solution.*

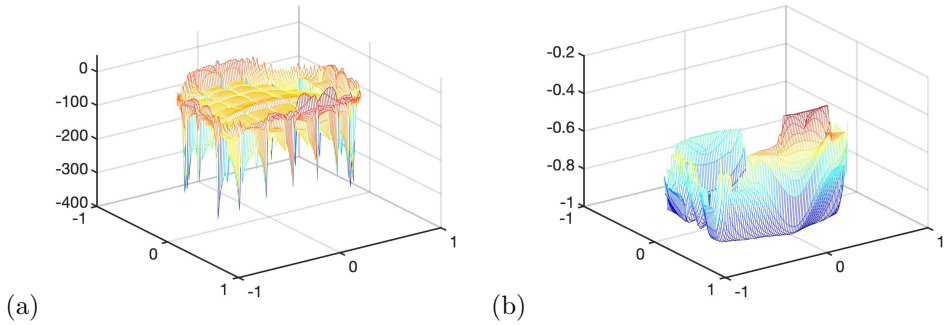

FIG. 12. *Example* 4.3. *The adjoint variables in the first iteration.* (a) *The sum of the original adjoint variables from all sources.* (b) *The sum of the proposed normalized adjoint variables from all sources.*

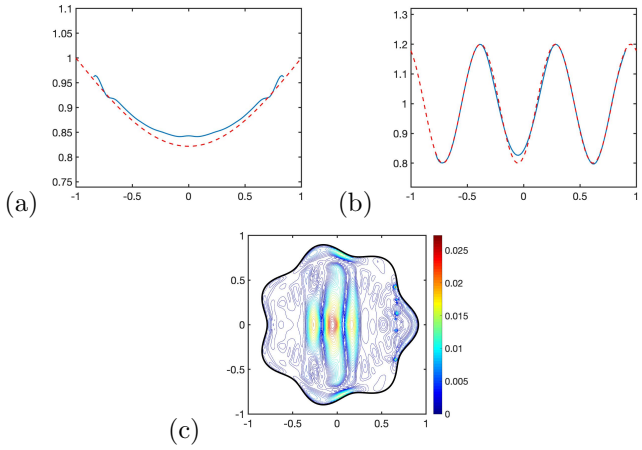

FIG. 13. *Example* 4.3. *Seven-folded star-shaped domain. Twenty sources are located uniformly on a circle of radius* 0.7. *The inverted solution is plotted in a blue solid line, while the exact solution is shown in the red dashed line.* (a) *The cross section of the solution along* $x = 0$. (b) *The cross section of the solution along* $y = 0$. (c) *The contour plot of the absolute error in the solution.*

formulation, the normalized approach is able to remove the singularity in the L^1-based adjoint variable.

Our algorithm for irregular domains can be easily applied to other shapes of the domain Ω_p. In Figure 13, we replace the circular domain by a seven-folded star-shaped domain with the boundary parameterized by $r = (1 + \epsilon \cos 7\theta)r_0$ with $r_0 = 0.85$ and the magnitude of perturbation $\epsilon = 0.075$. The overall reconstruction is still reasonably accurate.

4.4. A three-dimensional model. In this example, we consider a three-dimensional case, where the velocity model is given by

$$c(x, y, z) = 3 - \frac{1}{2}\exp\left(-\frac{x^2 + (y + 0.5)^2 + z^2}{0.5^2}\right) - \exp\left(-\frac{x^2 + (y - 0.25)^2 + x^2}{0.5^2}\right).$$

We consider inverting the velocity inside a sphere of radius $R_\Omega = 0.75$. Similar to all previous examples, we assume that we are given perfect measurements on the sphere R_Ω whenever needed in the algorithm. Ten sources are located uniformly on a sphere of radius $R_s = 0.6$. Such a uniform distribution is obtained by the solution of the so-called Thomson problem which tries to put N electrons on the surface of a sphere that minimizes the electrostatic potential energy governed by the Coulomb's law [44]. In this example, we consider $N = 10$ sources. These locations are explicitly known and the corresponding polyhedron is the so-called gyroelongated square di-pyramid. Figure 14 shows the initial condition and an intermediate solution and the converged inverted velocity of the model. As we can see, the maximum absolute error is dropped from close to 0.8 initially to 0.014 in the final solution.

4.5. Ultrasound CT time-of-flight datasets. In this example, we apply our algorithm to two time-of-flight (TOF) datasets from an ultrasound computed tomography (USCT) phantom experiment [21], where the TOF data are picked from simulated sonograms by using two different methods: one is based on the Akaike information criteria (AIC) picker method, and the other the differential cross-correlation

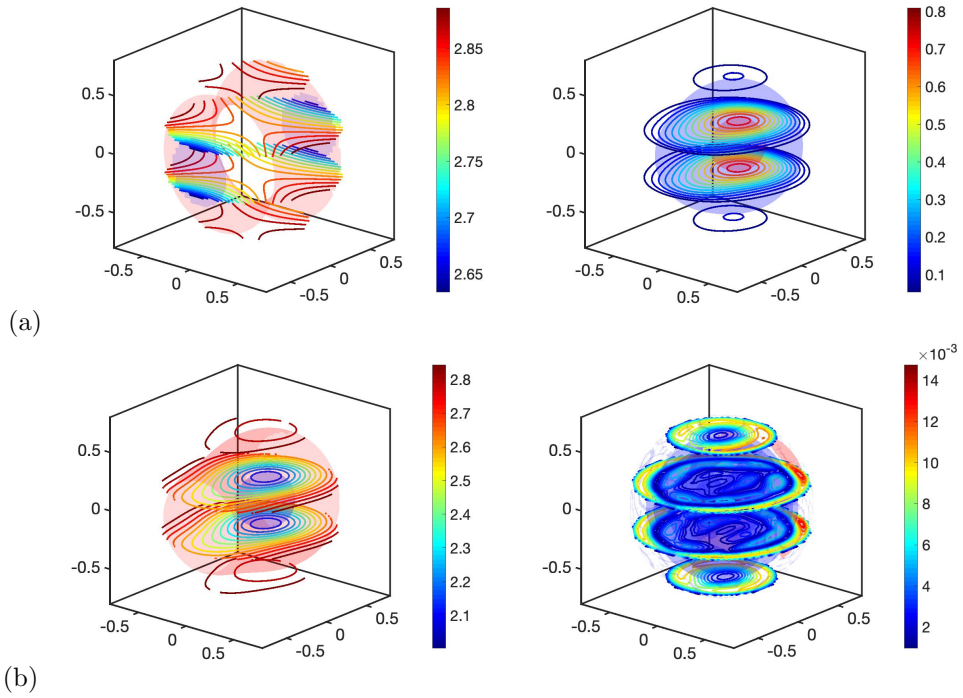

FIG. 14. *Example* 4.4. *Ten sources are located uniformly on a sphere of radius* 0.6. (a) *The initial velocity and the corresponding error in the initial condition.* (b) *The final inverted velocity and its corresponding error.*

(DXC) method, yielding two TOF datasets. We will apply our algorithm to both datasets.

First, we consider the TOF data from the AIC picker method. The two-dimensional USCT system consists of a circular transducer array of radius 110.0mm. The array consists of 1024 equally spaced transducers. In polar coordinates, the angular difference between two consecutive transducers is $2\pi/1024$. The speed of sound experimental phantom is shown in Figure 15, which contains several small objects with sharp changes in the intensity. A pulse wave is emitted by each transducer located on the circle plotted in a dashed line and received by all other transducers. That is, every transmitter is also a receiver, so this will generate 1024 sets of TOF data corresponding to 1024 transducers (sources). To better visualize the recovered solution in the following numerical results, we only concentrate on the inner region near the phantom in the squared region marked by solid black lines as shown in Figure 15(a).

To apply our algorithm to this dataset, we subsample from these 1024 sets of measurements to obtain two subsets: one containing 256 transducers and the other 512 transducers, respectively. Figure 16 shows our inverted solutions based on the L^1 mismatch functional and the normalized adjoint variables, where we have solved the eikonal and adjoint state equations with different mesh sizes. To compare with the synthetic phantom, we have also plotted the contour lines of the exact solution on top of our numerical solutions.

Figures 16(a) and (b) show the tomography results for the two subsets of the TOF data, where we have solved the eikonal and adjoint state equations using a

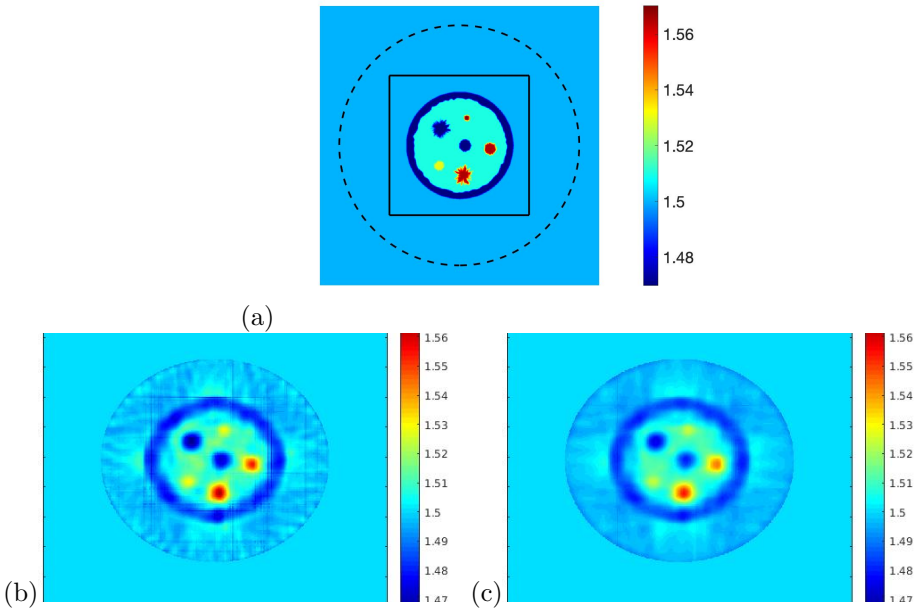

FIG. 15. *Example of USCT TOF data.* (a) *The true phantom data to be recovered. The transducers are located on the circle plotted using a black dashed line. To visualize our numerical results for this TOF experiment, we will concentrate only on the boxed zoom-in interior region. Reference solutions with* (b) 256 *transducers and* (c) 512 *transducers from* [21].

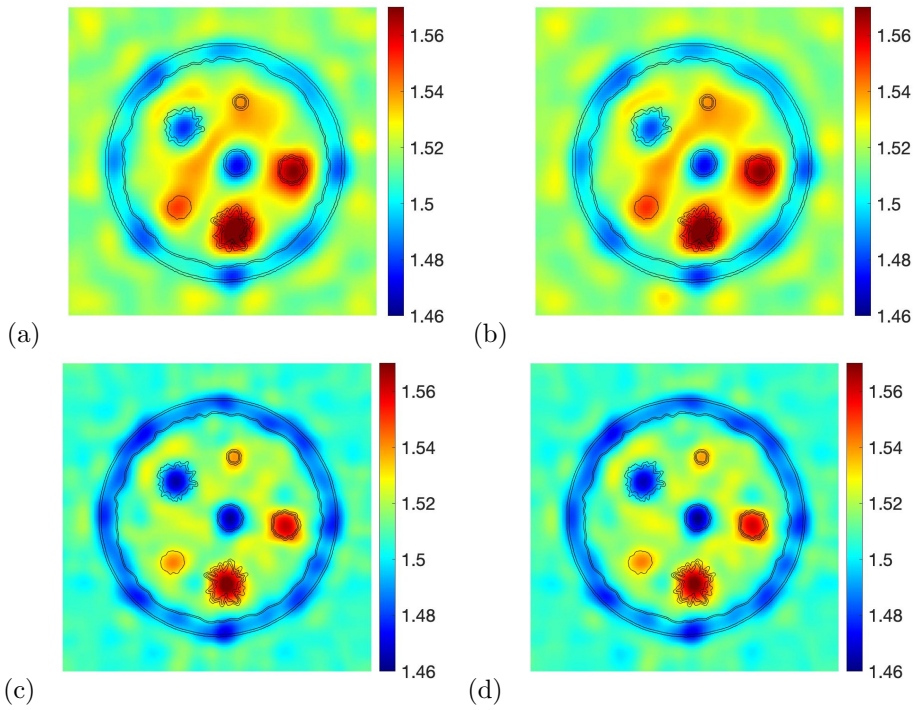

FIG. 16. *Example of USCT AIC-TOF data. The inverted velocity model with the* L^1 *misfit using* (a) 256 *transducers and* (b) 512 *transducers uniformly distributed along the circle of radius* 110*mm on a mesh of resolution* 257×257*;* (c)–(d) *follow the same setting as* (a)–(b) *but with resolution* 513×513*. We plot the contour of phantoms using black solid lines on the top of our solutions.*

low-resolution mesh of 257×257 points. Since the forward solver is only first-order accurate, the traveltime solution contains relatively large errors and, therefore, we are not able to obtain an accurate adjoint variable. As a result, the tomography solution has relatively low accuracy. However, as we increase the number of mesh points, the tomography resolution improves significantly, since the accuracy of the eikonal and adjoint variable improves. We have also noticed that increasing the number of transducers from 256 to 512 does not significantly improve the resolution of the inverted solution. Our approach can already effectively capture the overall structure of the phantom using a relatively small subset of the original data set. Figures 16(c) and (d) show the tomography results for the two subsets of the TOF data, where we have solved the eikonal and adjoint state equations using a high-resolution mesh of 513×513 points. To further illustrate the inversion results, the cross-section comparisons in Figure 17 show that our normalized adjoint-state method equipped with high resolution modeling and L^1 regularization is able to resolve fine details in the phantom structures.

We have also tested the robustness of our approach by adding a multiplicative Gaussian noise to the AIC-TOF data. Figures 18(a)–(b) show our inverted solutions based on the TOF data with 1% multiplicative Gaussian noise, while Figures 18(c)–(d) contain solutions from measurements with 2% multiplicative noise. We consider the case with only 256 transducers uniformly sampled along the circle of radius 110mm. Our inverted solutions are shown in Figure 18.

Figure 19 shows the tomography results based on the L^2 mismatch functional for the clean TOF data. Since the L^2 regularization imposes excessive regularity in the inverted solution, we do not expect these solutions to match with the phantom structures as well as those by the L^1 regularization since the phantom structures contain many sharp discontinuous interfaces.

Next, we consider the TOF data from the DXC method [21]. We have applied our approach to this data set by repeating the same experiments as described in Figures 16 and 19. Figure 20 shows our inverted solutions using both L^1 and L^2 regularizations computed on the fine mesh of resolution 513×513. To further illustrate the inversion results, the cross-section comparisons in Figure 21 show that our normalized adjoint-state method equipped with high resolution modeling and L^1 regularization is able to resolve fine details in the phantom structures.

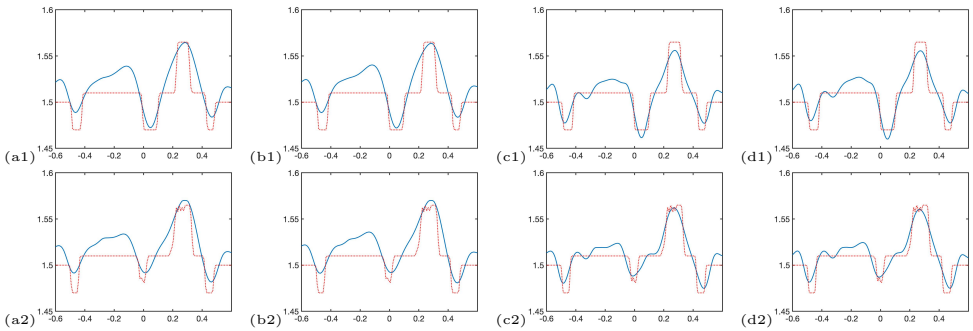

FIG. 17. *Example of USCT AIC-TOF data. The inverted velocity model with the L^1 misfit. Cross-sections of the solutions in Figure* 16 *along* (a1)–(d1) $y = 0$ *and* (a2)–(d2) $x = 0$. (a1)–(b1) *and* (a2)–(b2) *are from the* 257×257 *mesh;* (c1)–(d1) *and* (c2)–(d2) *are from the* 513×513 *mesh. The exact phantom is plotted in red dashed lines and our inverted solutions are plotted in blue solid lines.*

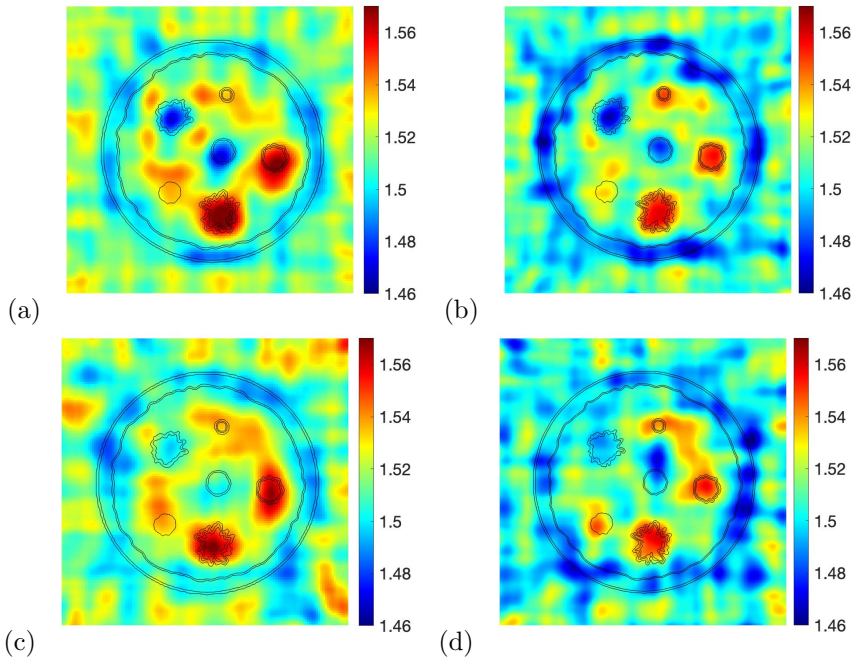

FIG. 18. *Example of USCT AIC-TOF data. The inverted velocity model from measurements containing* 1% *multiplicative Gaussian noise with the* L^1 *misfit using* 256 *transducers uniformly distributed along the circle of radius* 110*mm on a mesh of resolutions* (a) 257×257 *and* (b) 513×513*, respectively;* (c)–(d) *follow the same setting as* (a)–(b) *but the measurements contain* 2% *multiplicative Gaussian noise. We plot the contour of phantoms using black solid lines on the top of our solutions.*

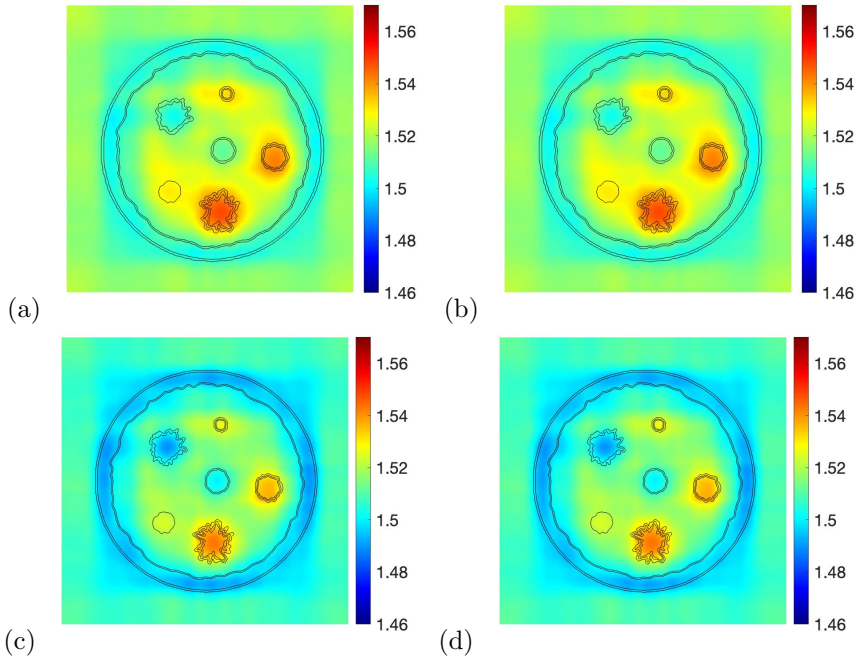

FIG. 19. *Example of USCT AIC-TOF data. The inverted velocity model with the* L^2 *misfit using* (a) 256 *transducers and* (b) 512 *transducers uniformly distributed along the circle of radius* 110*mm on a mesh of resolution* 257×257*;* (c)–(d) *follow the same setting as* (a)–(b) *but with resolution* 513×513*. We plot the contour of the phantom using black solid lines on the top of our solutions.*

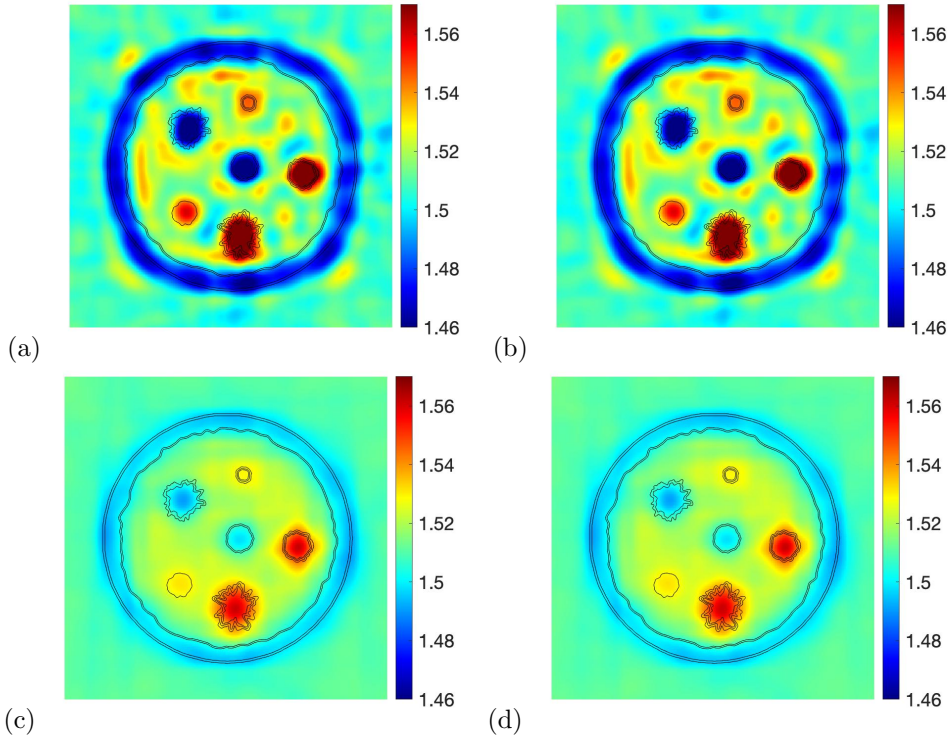

FIG. 20. *Example of USCT DXC-TOF data. The inverted velocity model with the* L^1 *misfit using* (a) 256 *transducers and* (b) 512 *transducers uniformly distributed along the circle of radius* 110*mm on a mesh of resolution* 513×513*;* (c)–(d) *follow the same setting as* (a)–(b) *but with the* L^2 *regularization.*

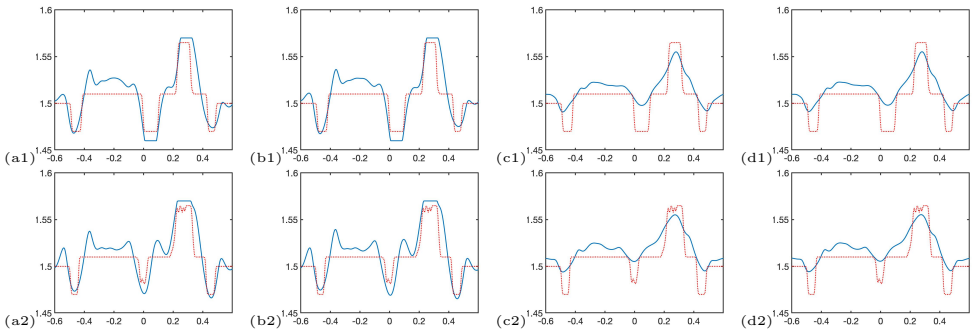

FIG. 21. *Example of USCT DXC-TOF data. The inverted velocity model with* L^1 *and* L^2 *misfits on the* 513×513 *mesh. Cross sections of the solutions in Figure* 20 *along* (a1)–(d1) $y = 0$ *and* (a2)–(d2) $x = 0$. (a1)–(b1) *and* (a2)–(b2) *are from the* L^1 *misfit;* (c1)–(d1) *and* (c2)–(d2) *are from the* L^2 *misfit. The exact phantom is plotted in red dashed lines and our inverted solutions are plotted in blue solid lines.*

5. Conclusion. We have developed a new algorithm to carry out the adjoint-state first-arrival traveltime tomography in irregular computational domains. The classical singular adjoint variable due to the point source is normalized to remove

such singular behavior, which is accomplished by solving another adjoint-state equation. We also developed an easy-to-implement finite-difference algorithm to carry out eikonal-based first-arrival traveltime tomography in irregular domains. Numerical examples demonstrate that the new method works extremely well.

REFERENCES

[1] C. Ammon and J. Vidale, *Tomography without rays*, Bull. Seis. Soc. Am., 83 (1993), pp. 509–528.

[2] G. S. Avila and J. B. Keller, *The high-frequency asymptotic field of a point source in an inhomogeneous medium*, Commun. Pure Appl. Math., 16 (1963), pp. 363–381.

[3] A. Benaichouche, M. Noble, and A. Gesret, *First Arrival Traveltime Tomography using the Fast Marching Method and the Adjoint State Technique*, in Expanded Abstracts, EAGE, 2015, pp. 1–5.

[4] M. Boue and P. Dupuis, *Markov chain approximations for deterministic control problems with affine dynamics and quadratic costs in the control*, SIAM J. Numer. Anal., 36 (1999), pp. 667–695.

[5] S. Chen, B. Merriman, S. Osher, and P. Smereka, *A simple level set method for solving Stefan problems*, J. Comput. Phys., 135 (1997), pp. 8–29.

[6] W. Chen, C. Chou, and C. Kao, *Lax-Friedrichs fast sweeping methods for steady state problems for hyperbolic conservation laws*, J. Comput. Phys., 234 (2013), pp. 452–471.

[7] E. Chung, J. Qian, G. Uhlmann, and H. Zhao, *A new phase space method for recovering index of refraction from travel times*, Inverse Problems, 23 (2007), pp. 309–329.

[8] E. Chung, J. Qian, G. Uhlmann, and H. Zhao, *An adaptive phase space method with application to reflection traveltime tomography*, Inverse Problems, 27 (2011), 115002.

[9] M. G. Crandall and P. L. Lions, *Viscosity solutions of Hamilton-Jacobi equations*, Trans. Amer. Math. Soc., 277 (1983), pp. 1–42.

[10] M. G. Crandall and P. L. Lions, *Two approximations of solutions of Hamilton-Jacobi equations*, Math. Comp., 43 (1984), pp. 1–19.

[11] N. Duric, P. Littrup, A. Babkin, D. Chambers, S. Azevedo, A. Kalinin, R. Pevzner, M. Tokarev, E. Holsapple, O. Rama, and R. Duncan, *Development of ultrasound tomography for breast imaging: Technical assessment*, Med. Phys., 32 (2005), pp. 1375–1386.

[12] R. Glowinski, S. Leung, and J. Qian, *A penalization-regularization-operator splitting method for eikonal based traveltime tomography*, SIAM J. Imaging Sci., 8 (2015), pp. 1263–1292.

[13] R. Glowinski, S. Leung, and J. Qian, *Operator-splitting based fast sweeping methods for isotropic wave propagation in a moving fluid*, SIAM J. Sci. Comput., 38 (2016), pp. A1195–A1223.

[14] C. Huang, L. Nie, R. Schoonover, L. V. Wang, and M. A. Anastasio, *Photoacoustic computed tomography correcting for heterogeneity and attenuation*, J. Biomedical Optics, 17 (2012), 061211.

[15] J.-W. Huang and G. Bellefleur, *Joint transmission and reflection traveltime tomography using the fast sweeping method and the adjoint-state technique*, Geophys. J. Internat., 188 (2012), pp. 570–582.

[16] C. Kao, S. Osher, and J. Qian, *Lax-Friedrichs sweeping schemes for static Hamilton-Jacobi equations*, J. Comput. Phys., 196 (2004), pp. 367–391.

[17] C. Y. Kao, S. Osher, and J. Qian, *Legendre transform based fast sweeping methods for static Hamilton-Jacobi equations on triangulated meshes*, J. Comput. Phys., 227 (2008), pp. 10209–10225.

[18] S. Leung and J. Qian, *A transmission tomography problem based on multiple arrivals from paraxial Liouville equations*, in Expanded Abstracts, SEG 75th Annual Meeting, 2005.

[19] S. Leung and J. Qian, *An adjoint state method for three-dimensional transmission traveltime tomography using first-arrivals*, Commun. Math. Sci., 4 (2006), pp. 249–266.

[20] S. Leung and J. Qian, *Transmission traveltime tomography based on paraxial Liouville equations and level set formulations*, Inverse Problems, 23 (2007), pp. 799–821.

[21] F. Li, U. Villa, J. Poudel, and M. Annastasio, *Time of Flight Picking from Simulated Sonograms*, Tech. report, Department of Bioengineering, University of Illinois at Urbana-Champaign, 2019.

[22] W. Li and S. Leung, *A fast local level set adjoint state method for first arrival transmission traveltime tomography with discontinuous slowness*, Geophys. J. Internat., 195 (2013), pp. 582–596.

[23] W. Li, S. Leung, and J. Qian, *A level-set adjoint-state method for crosswell transmission-reflection traveltime tomography*, Geophys. J. Internat., 199 (2014), pp. 348–367.
[24] W. Li and J. Qian, *Newton-type Gauss–Seidel Lax–Friedrichs high-order fast sweeping methods for solving generalized eikonal equations at large-scale discretization*, Comput. Math. Appl., 79 (2020), pp. 1222–1239.
[25] P. L. Lions, *Generalized Solutions of Hamilton-Jacobi Equations*, Pitman, Boston, 1982.
[26] W. Lu, J. Qian, and R. Burridge, *Babich's expansion and the fast Huygens sweeping method for the Helmholtz wave equation at high frequencies*, J. Comput. Phys., 313 (2016), pp. 478–510.
[27] R. Michel, *Sur la rigidite imposee par la longueur des geodesiques [On the rigidity imposed by the length of geodesics]*, Invent. Math., 65 (1981), pp. 71–83.
[28] R. G. Mukhometov, *The reconstruction problem of a two-dimensional Riemannian metric, and integral geometry* (in Russian), Dokl. Akad. Nauk SSSR, 232 (1977), pp. 32–35.
[29] R. G. Mukhometov, *On a problem of reconstructing Riemannian metrics*, Siberian Math. J., 22 (1982), pp. 420–433.
[30] G. Nolet, *A Breviary of Seismic Tomography*, Cambridge University Press, Cambridge, UK, 2009.
[31] L. Pestov and G. Uhlmann, *Two dimensional compact simple Riemannian manifolds are boundary distance rigid*, Ann. of Math., 161 (2005), pp. 1093–1110.
[32] J. Qian and W. W. Symes, *Adaptive finite difference method for traveltime and amplitude*, Geophysics, 67 (2002), pp. 167–176.
[33] J. Qian, Y. T. Zhang, and H. K. Zhao, *Fast sweeping methods for eikonal equations on triangulated meshes*, SIAM J. Numer. Analy., 45 (2007), pp. 83–107.
[34] J. Qian, Y. T. Zhang, and H. K. Zhao, *Fast sweeping methods for static convex Hamilton-Jacobi equations*, J. Sci. Comput., 31 (2007), pp. 237–271.
[35] F. Qin, Y. Luo, K. B. Olsen, W. Cai, and G. T. Schuster, *Finite difference solution of the eikonal equation along expanding wavefronts*, Geophysics, 57 (1992), pp. 478–487.
[36] A. Sei and W. W. Symes, *Gradient calculation of the traveltime cost function without ray tracing*, in Expanded Abstracts, SEG 65th Annual Meeting, Tulsa, OK, 1994, pp. 1351–1354.
[37] A. Sei and W. W. Symes, *Convergent finite-difference traveltime gradient for tomography*, in Expanded Abstracts, SEG 66th Annual Meeting, Tulsa, OK, 1995, pp. 1258–1261.
[38] J. A. Sethian and A. M. Popovici, *3-D traveltime computation using the fast marching method*, Geophysics, 64 (1999), pp. 516–523.
[39] P. Stefanov and G. Uhlmann, *Boundary rigidity and stability for generic simple metrics*, J. Amer. Math. Soc., 18 (2005), pp. 975–1003.
[40] P. Stefanov and G. Uhlmann, *Integral geometry of tensor fields on a class of non-simple Riemannian manifolds*, Amer. J. Math., 130 (2008), pp. 239–268.
[41] P. Stefanov and G. Uhlmann, *Local lens rigidity with incomplete data for a class of non-simple Riemannian manifolds*, J. Differential Geom., 82 (2009), pp. 383–409.
[42] W. W. Symes and J. Qian, *A slowness matching Eulerian method for multivalued solutions of eikonal equations*, J. Sci. Comput., 19 (2003), pp. 501–526.
[43] C. Taillandier, M. Noble, H. Chauris, and H. Calandra, *First-arrival traveltime tomography based on the adjoint-state method*, Geophysics, 74 (2009), pp. WCB1–WCB10.
[44] J. Thomson, *On the structure of the atom: An investigation of the stability and periods of oscillation of a number of corpuscles arranged at equal intervals around the circumference of a circle; with application of the results to the theory of atomic structure*, Philosophical Magazine, 7 (1904), pp. 237–265.
[45] R. Tsai, L.-T. Cheng, S. J. Osher, and H. K. Zhao, *Fast sweeping method for a class of Hamilton-Jacobi equations*, SIAM J. Numer. Anal., 41 (2003), pp. 673–694.
[46] J. van Trier and W. W. Symes, *Upwind finite-difference calculation of traveltimes*, Geophysics, 56 (1991), pp. 812–821.
[47] J. Vidale, *Finite-difference calculation of travel times*, Bull. Seis. Soc. Am., 78 (1988), pp. 2062–2076.
[48] B. S. White, *The stochastic caustic*, SIAM J. Appl. Math., 44 (1984), pp. 127–149.
[49] T. Wong and S. Leung, *A fast sweeping method for eikonal equations on implicit surfaces*, J. Sci. Comput., 67 (2016), pp. 837–859.
[50] Y. Zhang, H. Zhao, and J. Qian, *High order fast sweeping methods for static Hamilton-Jacobi eqations*, J. Sci. Comput., 29 (2006), pp. 25–56.
[51] H. Zhao, S. Osher, B. Merriman, and M. Kang, *Implicit and non-parametric shape reconstruction from unorganized points using variational level set method*, Computer Vision and Image Understanding, 80 (2000), pp. 295–319.

[52] H. K. Zhao, *Fast sweeping method for eikonal equations*, Math. Comp., 74 (2005), pp. 603–627.
[53] H.-K. Zhao and Y. Zhong, *A hybrid adaptive phase space method for reflection traveltime tomography*, SIAM J. Imaging Sci., 12 (2019), pp. 28–53.